ACS WFC CCD Radiation Test: The Radiation Environment

Michael R. Jones
Space Telescope Science Institute
May 15, 2000

ABSTRACT

The space environment is a complex, orbit dependent phenomenon. Regardless of orbit, the external surfaces of a spacecraft will be exposed to photons, charged particles and solid particles such as micrometeoroids. Vehicles in low earth orbit (LEO) must be designed to withstand additional environmental hazards such as hyper-velocity impacts by man-made orbital debris and erosion of external surfaces by naturally occurring atomic oxygen. CCD detectors are particularly vulnerable to damage by ionizing radiation. This document summarizes the modeling and analysis that was performed to determine the appropriate exposure level for ground testing of the Advanced Camera for Surveys (ACS) Wide Field Channel (WFC) Charge-Coupled Device (CCD) detector.

1. Introduction

Radiation damage effects in CCD imagers have been studied in the laboratory for upwards of 30 years. Good quality long-term measurements of the on-orbit degradation of CCD detectors in the space environment have also recently become available. Ground test data and on-orbit measurements are consistent in showing that CCD imagers are highly susceptible to radiation damage.

A comprehensive discussion of the types of radiation damage known to occur in CCDs is beyond the scope of this document. Excellent survey papers on the subject can be found in the literature [1,2]. Papers that provide an overview of the space radiation environment and the impact of radiation on spacecraft systems have also been published [3,4]. Readers who desire to explore these topics in more depth are encouraged to read the cited references.

Spacecraft in low earth orbit at all inclinations are exposed to electrons and protons trapped in the Van Allen radiation belts. The accumulated exposure to trapped particles is

dominated by passage through the South Atlantic Anomaly (SAA). Unlike trapped radiation, exposure to solar coronal mass ejection (CME) protons is inclination dependent. A vehicle in a high inclination orbit will be exposed to CME protons as it flies through the polar auroral regions of the geomagnetic field. For the low inclination 28.5 degree HST orbit, attenuation by the geomagnetic field effectively shields the spacecraft from CME protons. Justification for neglecting CME protons in the ACS equivalent fluence calculation will be presented below.

In addition to trapped particles and CME protons, a LEO spacecraft is subjected to a low-level galactic cosmic ray (GCR) flux. GCR heavy ions and high energy trapped protons cause single event upsets (SEUs) and single event latchups (SELs) in microelectronics as well as false signals in CCD detectors. The contribution of GCRs to the total ionizing dose (TID) deposited in a CCD is small compared to the TID deposited by trapped charged particles. For this reason, GCRs have been ignored in the calculation of the accelerator exposure level for the ACS radiation test program.

Radiation damage mechanisms in CCD imagers are divided into two general categories: TID effects and displacement damage effects. TID refers to the ionizing energy deposited by the passage of a charged particle (or photon) through a material such as silicon. Generation of electron-hole pairs in the gate oxide or field oxide of a CCD can give rise to flat-band shift and/or surface states at the silicon-oxide interface. Displacement damage refers to the introduction of defects in the silicon lattice. A charged particle or a photon can dislodge a silicon atom by disrupting the covalent bonds that it shares with neighboring atoms in the lattice. The displaced atom can come to rest in the interstitial space between atoms. A phosphorous atom in the buried n-channel of the CCD can pair up with a vacancy to form an E-center defect. Vacancies can pair up to form a divacancy defect. An oxygen impurity atom may combine with a vacancy to form an A-center defect. Irrespective of the nature of the defect, only a small fraction of the total number of radiation induced displacements result in permanent electrically active defects in the silicon lattice. Table 1 summarizes TID and displacement damage effects in CCD imagers.

Dark current and charge transfer efficiency (CTE) both degrade with time in the space radiation environment. Because of the relatively large format of the WFC CCD imagers (2kx4k, 2 imagers per FPA), CTE degradation was the primary focus of the ACS radiation test program. Defects in the silicon lattice cause localized states in the band gap. The E-center P-V defect, for example, gives rise to a state at an energy of 0.44 eV below the bottom of the conduction band [5]. In general, an electron in the conduction band is captured in the potential well of the defect on a time scale short relative to the pixel transfer time typical of scientific applications. In the temperature regime usually chosen for science operation, -80 °C to -100 °C, the time scale for liberation of an electron captured in a trap can be large compared to the pixel transfer time. Charge trapping and release is the physi-

cal cause of time dependent image smear and photometric error in CCD imagers exposed to the radiation environment.

2. Environment Modeling Methodology

Modeling of the trapped radiation environment for the ACS radiation test program was performed using the empirical NASA AP-8 [6] and AE-8 [7] particle flux maps. Known deficiencies exist in these flux maps. Both models were accurate at the time of publication, but temporal changes in the position and strength of the geodipole moment have now become large enough to introduce systematic errors in the maps [8]. This has been demonstrated specifically for HST by Vampola et al. [9]. Vampola et al. have shown a lack of longitudinal correlation between the AP-8-MIN (solar mininum) predictions and measured SEU events in the HST solid-state recorder (SSR).

Although forward progress is being made in developing a new generation of generally applicable models of the radiation belts, Daly et al. correctly assert that the AP-8/AE-8 models are still the de-facto standard. From shuttle measurements and analysis of materials flown aboard the Long Duration Exposure Facility (LDEF), Daly et al. estimate that the ratio of measured to predicted fluxes in the SAA is 1.55-2.3. The systematic error is likely to be orbit dependent. For this reason, the ACS flux calculations have not been scaled either by the shuttle ratio or by the LDEF ratio.

The trapped electron and trapped proton fluxes depend on the solar cycle. The trapped electron flux is correlated with the level of solar activity. By contrast, the trapped proton flux is anti-correlated with the phase of the solar cycle. For this reason, separate AP-8 and AE-8 flux maps have been developed for solar minimum and solar maximum. A well accepted methodology for interpolation between the solar minimum and solar maximum flux maps has not yet been devised. Interpolation between the solar maximum and solar minimum flux maps has not been attempted in the ACS radiation environment modeling.

Extraction and orbit averaging of the flux maps was executed with software written or modified by the author. The trajectory of the spacecraft was computed using the NORAD implementation of the SGP4 ephemeris model [10]. For a given orbit position, the McIlwain L parameter and the normalized geomagnetic field strength B/B0 was calculated using the 1995 International Geomagnetic Reference Field model (IGRF95) [11]. For extraction of the flux maps, the National Space Science Data Center (NSSDC) RADBELT computational engine was employed (Dieter Bilitza, GSFC, 1988). SGP4, IGRF95 and RADBELT, with front end modifications written by the author, have been integrated into a software package called TRAPRAP. TRAPRAD properly detects and rejects all flux values flagged by RADBELT as unreliable. The particle spectra presented in this document have not been smoothed.

An altitude and orbit inclination of 600 km and 28.5 degrees, respectively, was assumed for all calculations. Second order perturbations in the SGP4 ephemeris model were set equal to zero. The orbit trajectory was sampled with a time resolution of 10 seconds. Averaging of the trapped particle fluxes was performed over 100 orbits.

3. Trapped Proton Environment

Differential trapped proton spectra for the HST orbit computed with TRAPRAD are shown in Figure 1. The average daily flux at solar minimum (AP-8-MIN flux map) is greater than the flux at solar maximum (AP-8-MAX flux map). This result is consistent with the anti-correlation between the proton flux and the phase of the solar cycle.

Systematic errors most likely exist in the TRAPRAD simulated fluxes. Consistent with the recommendations of D. Bilitza (RADBELT, 1988), epochs of 1964 for AP-8-MIN and 1970 for AP-8-MAX were chosen for the IGRF95 L and B/B0 calculations. Until very recently, there has been disagreement in the radiation effects community regarding the proper procedure for extraction of the AP-8/AE-8 flux maps. The correct procedure has now been published by Daly et al. [8]. Reconstruction of the AP-8-MIN flux map should be performed using the Jensen and Cain field model (JC-60) [12]. The GSFC-12/66 field model extrapolated to epoch 1970 should be used for extraction of the AP-8-MAX flux map. The magnitude of the error introduced into the flux calculations through the use of IGRF95 instead of JC-60 and GSFC-12/66 is unknown. JC-60 has been procured by the author and will be incorporated in TRAPRAD for future work.

An error in the NSSDC AP-8-MIN flux map was identified by Heynderickx and Beliaev in 1995 [13]. TRAPRAD utilizes the corrected version of the AP-8-MIN map.

4. Trapped Electron Environment

Figure 2 shows the differential TRAPRAD AE-8-MIN (solar minimum) and AE-8-MAX (solar maximum) average daily fluxes for the HST orbit. As one would expect from the correlation between the trapped electron environment and the level of solar activity, AE-8-MAX yields the highest flux. Note that the electron spectrum is not as hard as the proton spectrum. It is for this reason that trapped electrons are usually stopped by the shielding typically employed for radiation sensitive systems in spacecraft.

As with the trapped proton calculations, the TRAPRAD electron fluxes are likely to contain systematic errors because of the use of the IGRF95 geomagnetic field model. Although the epochs used in the IGRF95 calculations are in accord with the recommendations of Bilitza, Daly et al. state that the correct procedure for reconstruction of the AE-8 flux maps is to use JC-60. Future TRAPRAD flux calculations will be performed with JC-60.

5. CME Proton Environment

CME protons are not a threat to a spacecraft in a low inclination low earth orbit. This is the reason for ignoring CME protons in the definition of the exposure level for the ACS CCD radiation test program. In this section, quantitative arguements are presented to justify the decision to omit CME protons.

Ionized CME protons injected into the magnetosphere are deflected by the Lorentz force. For satellites in low earth orbit, the geomagnetic field attenuates the CME proton flux. Calculation of the attenuated differential flux (or fluence) proceeds as follows:

$$F'(E) = T(R(E)) \times F(E)$$

$$R(E) = \sqrt{E^2 + 2EM_o c^2}$$

where E is the proton kinetic energy and M_o is equal to 1 AMU or 931.5016 MeV/c^2. *R(E)* is the rigidity of the proton. *T(R(E))* is the geomagnetic attenuation function.

An orbit averaged calculation of *T* for HST is shown in Figure 3. The geomagnetic attenuation for the EOS AM-1 (TERRA) spacecraft is also shown for comparison. TERRA flies in a circular, 705 km, 98.2 degree inclination orbit. These calculations were executed with the GTRN module of CREME96 [14] for a disturbed ("stormy") magnetospheric environment. Note that the geomagnetic cutoff occurs at a much higher energy for HST. Unlike HST, TERRA flies through the auroral region where the field lines due to the geodipole are nearly perpendicular to the surface of the earth. Deflection of CME protons in the polar cusp is lower than at low inclination because the cross-product in the Lorentz force is small. TERRA is therefore exposed to CME protons in the polar regions. This is reflected by the lower cutoff energy in the transmission function.

Figure 4 graphically illustrates the effect of geomagnetic attenuation. Attenuated CME spectra using the CREME96 Solar-Energetic Particle ("flare") Worst Day Model are shown for HST and TERRA. The effect of exposure to CME protons in the polar auroral regions can clearly be seen. Comparison of the worst-case AP-8-MIN HST trapped proton flux to the HST CME proton flux shows why it is reasonable to disregard CME protons in the ACS equivalent exposure calculation.

6. Total Ionizing Dose (TID)

In this document, total ionizing dose will be quantified in units of rads (radiation absorbed dose). One rad is equal to 100 ergs of deposited ionizing energy per gram of matter. It must be clearly understood that the quantity of ionizing radiation that corresponds to 1 rad of TID depends on the material. For a given specie of ionizing radiation, the electronic stopping power will depend on the material. All TID calculations for silicon are

presented in units of rad (Si). Similarly, for another semiconductor material such as GaAs the correct unit is rad (GaAs).

Calculation of the TID for the HST environment has been accomplished using SHIELDOSE-2 [15,16]. SHIELDOSE-2 is a mature and widely accepted code for the calculation of TID in the omni-directional, spread spectrum space radiation environment. Contributions to the TID by protons (trapped and CME, where appropriate), trapped electrons and electron Bremsstrahlung resulting from transport through shielding are included.

A curve of Si TID versus 4π spherical aluminum shielding thickness for the HST environment is shown in Figure 5. The 2.5 year worst-case calculation has been performed using the solar minimum spectra (AP-8-MIN/AE-8-MIN). Note that trapped protons dominate the TID for shielding thicknesses exceeding ~100 mils. This is consistent with what one would expect based on the range of electrons in aluminum, as depicted in Figure 6 [17]. For an equivalent aluminum shielding thickness of 1 inch, the TID is approximately 470 rad (Si).

7. Non-Ionizing Energy Loss (NIEL)

Non-ionizing energy loss is proportional to bulk displacement damage [18]. NIEL calculations are available for electrons, protons, neutrons and photons in silicon [19]. A procedure for the application of NIEL equivalence to CCD imagers exposed to the mixed specie radiation environment has also been defined [20]. Since NIEL is proportional to bulk displacement damage, NIEL equivalence can be used to determine the accelerator fluence necessary to simulate on-orbit CTE degradation.

Figure 7 shows the NIEL for silicon taken from Van Ginneken. NIEL is a measure of non-ionizing energy loss per unit areal density. The product of NIEL and the mass density of the material yields the non-ionizing energy loss per unit linear length along the path of the particle (or photon). Note that the NIEL of photons is much smaller than the NIEL of protons. Electron Bremsstahlung can therefore be neglected in the NIEL equivalence computation.

The contract end item (CEI) specification for the WFC CCD detector calls only for adequate radiation shielding to meet a performance requirement of $\leq$10% signal loss after 5 years on-orbit. In Ball SER ACS-CCD-019 [21], a system requirement for the WFC CCD of 1 inch of aluminum or aluminum equivalent shielding over 99% of the 4π FOV is specified. Flow-down of the Ball system requirement from the CEI specification is not documented. Compliance with the Ball system requirement was demonstrated in the same SER through sector analysis. The sector analysis summed the contributions due to both intentional and incidental shielding mass only up to the minimum 1 inch system requirement. Significant effort would have been required by the author to trace the complete

shielding distribution surrounding the detector including the spacecraft. No attempt was made to perform sector analysis at this level.

Because the trapped electrons are stopped by the shielding, transport calculations are necessary only for the trapped protons. The NASA Langley Research Center BRYNTRN computer code (version BRYNTRN3 optimized for a PC platform) was employed for the proton transport calculations [22]. BRYNTRN is advantageous in that secondary particles generated by the transport of protons through the shielding are simulated. Exiting primary proton, secondary proton and secondary neutron differential spectra for 1 inch of spherical aluminum shielding are depicted in Figure 8. The secondary neutron flux has most likely been underestimated by modeling the shielding as pure aluminum. With the exception of the window, the detector housing is actually constructed of molybdenum and Alloy 42 (59 % Fe, 40 % Ni, 1 % trace elements). Secondary neutron production in high Z materials can be significantly higher than in aluminum. It should be noted that high Z materials can, to within a limited degree of fidelity, be modeled with BRYNTRN.

Figure 9 depicts the 2.5 year energy integrated NIEL damage spectra derived from the exiting BRYNTRN spectra:

$$D(E) = \int_{E}^{\infty} F(E) \times NIEL(E) dE$$

where *F(E)* is the exiting proton (or neutron) differential fluence and *NEIL(E)* is the per particle non-ionizing energy loss. For neutrons, the NIEL curve of Van Ginneken shown in Figure 7 was used. Updated NIEL calculations of Summers et al. and Dale et al. [23,24] were used for computation of the proton damage curves. The integrated damage curves are essentially asymptotic at 0.1 MeV. The total silicon NIEL is therefore the sum of the primary proton, secondary proton and secondary neutron NIEL, 1.29E+07 MeV/g.

For 1 inch of equivalent aluminum shielding, the calculations indicate that secondary neutrons contribute about 8% to the total displacement damage. This is certain to be an underestimate of the actual secondary neutron displacement damage since the atomic number of aluminum is lower than that of molybdenum and Alloy 42. As an example, Dale et al. [20] demonstrated that secondary neutrons dominate the total displacement damage for a tantalum shield thickness of 2.5 cm in the SAGE (705 km altitude, 97.4 degree inclination) trapped proton environment.

8. Accelerator Exposure

A curve of NIEL equivalent accelerator proton fluence versus accelerator energy can be computed as follows:

$$F_{acc}(E) = \frac{D_{pp}(0.1\text{ MeV}) + D_{sp}(0.1\text{ MeV}) + D_{np}(0.1\text{ MeV})}{NIEL_p(E)}$$

where $NIEL_p(E)$ is the per proton NIEL and $D(0.1\ MeV)$ is the asymptotic energy integrated damage calculated in the previous section. Subscripts *pp*, *sp* and *np* denote primary protons, secondary protons and secondary neutrons, respectively. The numerator is recognized as the total integrated damage NIEL, 1.29E+07 MeV/g. Figure 10 shows the 2.5 year accelerator fluence curve.

Irradiation of the devices was performed at the University of California, Davis Crocker Nuclear Laboratory cyclotron. The proton energy was 63 MeV. The decision to use this energy was dictated by the need to insert the CCDs into an integrated test schedule of other devices without retuning the accelerator (a potentially time consuming process). This is nevertheless an appropriate choice of energy since 63 MeV falls near the peak of the transported primary proton spectrum (Figure 8).

Uniform irradiation of the devices was accomplished by tilting the long axis of the CCD at an angle of 60 degrees relative to the collimated proton beam. Tilted in this manner, the projected area of the CCD relative to the beam is approximately 3.1 cm square. The spatial distribution of the beam is quite broad within a radius of 3 cm. Compared to the beam center, the fluence drops by only 3% at a radius of 2 cm [25]. Both the 2048 by 4096 array of pixels and the output amplifier structures are therefore well within the heart of the beam.

The exposure level for periods of time on-orbit other than 2.5 years was calculated by simple linear scaling of the 2.5 year NIEL equivalent accelerator fluence:

$$F_{acc}(T) = F_{acc}(2.5\text{ years}) \times \frac{T}{2.5}$$

where *T* is in years. Riess et al. [26] have studied the growth of cosmic ray deferred charge tails in dark frames taken with the STIS and WFPC2 CCD detectors. Cosmic ray tails in the STIS detector have grown at a roughly constant rate over a time span of ~2.5 years. By contrast, the rate of growth of the cosmic ray tails in the WFPC2 detectors over a period of ~5.5 years appears to be changing and may even be increasing with time. However, beginning with the launch of STIS the rates of growth of the cosmic ray tails in the WFPC2 and

STIS detectors, when corrected for the differences in system gain, are comparable. The cause of the apparent acceleration in the WFPC2 growth rate is not yet understood.

9. References

1. G.R. Hopkinson, *Radiation Effects on Solid State Imaging Devices,* Radiat. Phys. Chem., Vol. 43, No. 1/2, 1994.

2. James Janesick, George Soli, Tom Elliott and Stewart Collins, *The Effects of Proton Damage on Charge-Coupled Devices,* SPIE Electronic Imaging Science and Technology Conference, Charge-Coupled Devices and Solid State Optical Sensors II, Vol. 1147, February 1991.

3. E.G. Stassinopoulos and James P. Raymond, *The Space Radiation Environment for Electronics,* Proceedings of the IEEE, Vol. 76, No. 11, November 1988.

4. James D. Kinnison, Richard H. Maurer and Thomas M. Jordan, *Estimation of the Charged Particle Environment for Earth Orbits,* Johns Hopkins APL Technical Digest, Volume 11, Numbers 3 and 4, 1990.

5. A.D. Holland, *The Effect of Bulk Traps in Proton Irradiated EEV CCDs*, Nuc. Inst. Meth. Phys. Res., A326, 335-343, 1993.

6. D.W. Sawyer and J.I. Vette, *AP-8 Trapped Proton Environment for Solar Maximum and Minimum*, NSSDC/WDC-A-R&S 76-06, 1976.

7. J.I. Vette, *The AE-8 Trapped Electron Environment*, NSSDC/WDC-A-R&S 91-24, 1991.

8. E.J. Daly, J. Lemaire, D. Heynderickx and D.J. Rodgers, *Problems with Models of the Radiation Belts*, IEEE Trans. Nuc. Sci., Vol. 43, No. 2, April 1996.

9. A.L. Vampola, M. Lauriente, S. Huston and K. Pfitzer, *Validating the New SEE Low Altitude Proton Model*, Paper presented at the Conference on the High Radiation Background in Space (CHERBS), Snowmass, CO, July 23-24 1997.

10. Felix R. Hoots and Ronald L. Roehrich, *Project Space Track Report No. 3,* Aerospace Defense Center, Peterson AFB, CO, December 1988.

11. C.E. Barton, *International Geomagnetic Reference Field: The Seventh Generation*, J. Geomag. Geoelectr., Vol. 49, 123-148, 1997.

12. D.C. Jensen and J.C. Cain, *An Interim Geomagnetic Field,* J. Geophys. Res. 67, 3568, 1962.

13. D. Heynderickx and A. Beliaev, *Identification and Correction of an Error in the Distribution of the NASA Trapped Radiation Model AP-8 MIN*, J. Spacecraft and Rockets, Vol. 32, pp. 190-192, 1995.

14. Allan J. Tylka et al., *CREME96: A Revision of the Cosmic Ray Effects on Micro-Electronics Code*, IEEE Trans. Nuc. Sci., Vol. 44, No. 6, December 1997.

15. Stephen Seltzer, *SHIELDOSE: A Computer Code for Space-Shielding Radiation Dose Calculations*, NBS Technical Note 1116, May 1980.

16. S.M. Seltzer, *Updated Calculations for Routine Space-Shielding Radiation Dose Estimates: SHIELDOSE-2*, NIST Publication NISTIR 5477, 1994.

17. M.J. Berger and S.M. Seltzer, NASA SP-3012, 1964.

18. G.P. Summers, E.A. Burke, C.J. Dale, E.A. Wolicki, P.W. Marshall and M.A. Gehlhausen, *Correlation of Particle-Induced Displacement Damage in Silicon*, IEEE Trans. Nuc. Sci., Vol. NS-34, No. 6, December 1987.

19. A. Van Ginneken, *Non Ionizing Energy Deposition in Silicon for Radiation Damage Studies*, Fermi National Accelerator Laboratory report FN-522, October 1989.

20. Cheryl Dale, Paul Marshall, Brent Cummings, Louis Shamey and Andrew Holland, *Displacement Damage Effects in Mixed Particle Environments for Shielded Spacecraft CCDs*, IEEE Trans. Nuc. Sci., Vol. 40, No. 6, December 1993.

21. D. Feaver, *WFC CCD Radiation Shielding Analysis*, BATC SER ACS-CCD-019, March 1997.

22. J.W. Wilson, L.W. Townsend, J.E. Nealy, S.Y. Chun, B.S. Hong, W.W. Buck, S.L. Lamkin, B.D. Banapol, F. Khan and F.A. Cucinotta, *BRYNTRN: A Baryon Transport Model*, NASA Technical Paper 2887, March 1989.

23. Geoffrey P. Summers, Edward A. Burke, Philip Shapiro, Scott R. Messenger and Robert J. Walters, *Damage Correlations in Semiconductors exposed to Gamma, Electron and Proton Radiations*, IEEE Trans. Nuc. Sci., Vol. 40, No. 6, December 1993.

24. C.J. Dale, L. Chen, P.J. McNulty, P.W. Marshall and E.A. Burke, *A Comparison of Monte Carlo and Analytic Treatments of Displacement Damage in Si Microvolumes*, IEEE Trans. Nuc. Sci., Vol. 41, No. 6, December 1994.

25. Carlos M. Castaneda, *CNL Beam Counting and Quality Controls for the Radiation Effects Facility*, University of California at Davis Crocker Nuclear Laboratory report.

26. Adam Riess, John Biretta and Stefano Casertano, *Time Dependence of CTE from Cosmic Ray Tails*, Space Telescope Science Institute Instrument Science Report (ISR) WFPC2 99-04, 23 December 1999.

Effect	Damage Mechanism	Comment
flat-band voltage shift	TID	build up of hole density in gate oxide, positive space charge
birds-beak	TID	build up hole density in field (channel stop) oxide, increase in dark current, reduction of bloomed full well (BFW)
surface dark current	TID	increase in density of surface states, increase in dark current
bulk dark current	NIEL	intermediate energy states in forbidden band-gap, carrier hopping from valence band to conduction band, increase in mean dark current, increase in hot pixels, random telegraph signal (RTS)
surface CTE	TID	trapping of conduction band carriers at oxide-Si interface, increase in deferred charge
bulk CTE	NIEL	trapping of carriers by intermediate energy states in band-gap, increase in deferred charge
false signal	ionization	transient effect caused by electron-hole pair generation in Si, ‘cosmic-ray’ hits

Table 1. Summary of radiation damage effects in CCD imagers.

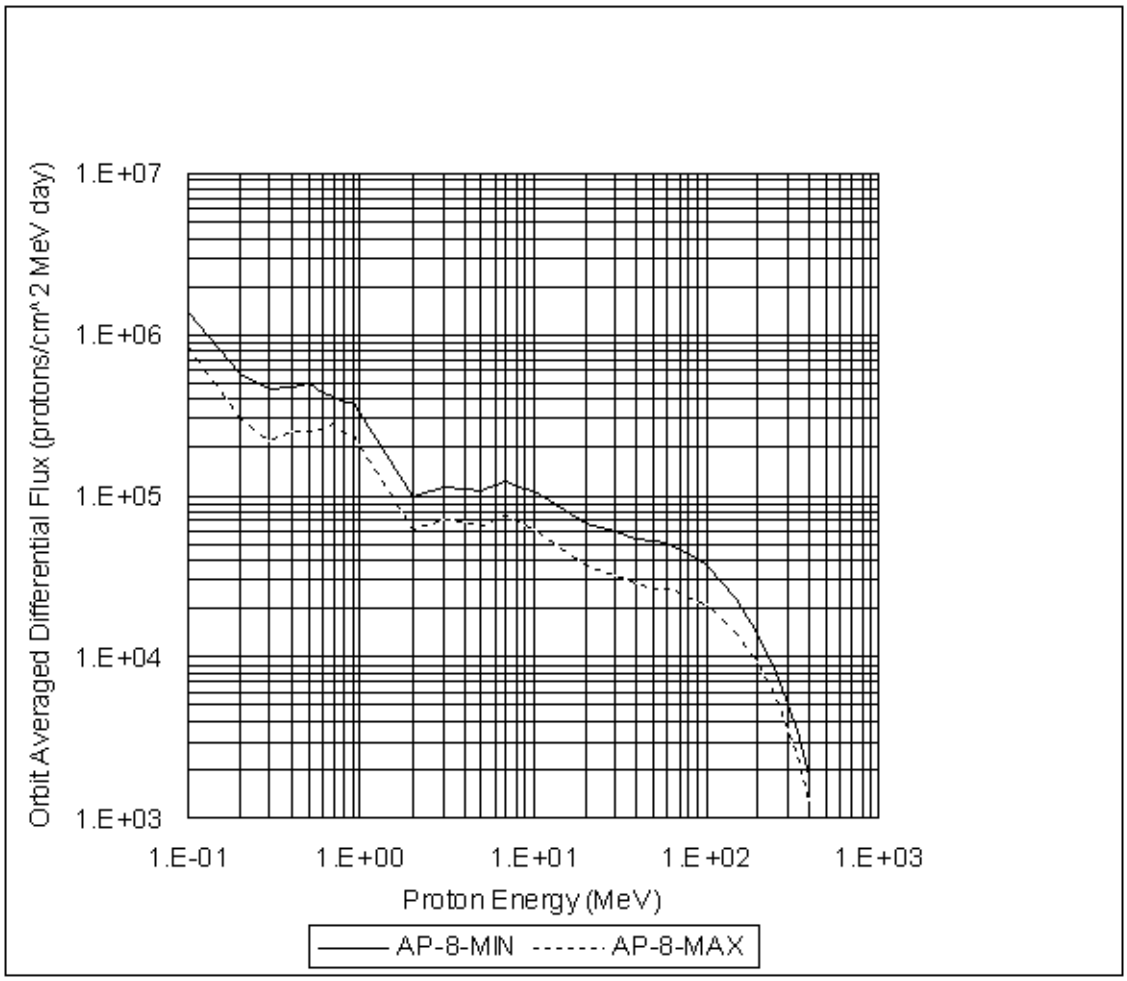

Figure 1: HST trapped proton spectra for solar maximum and solar minimum.

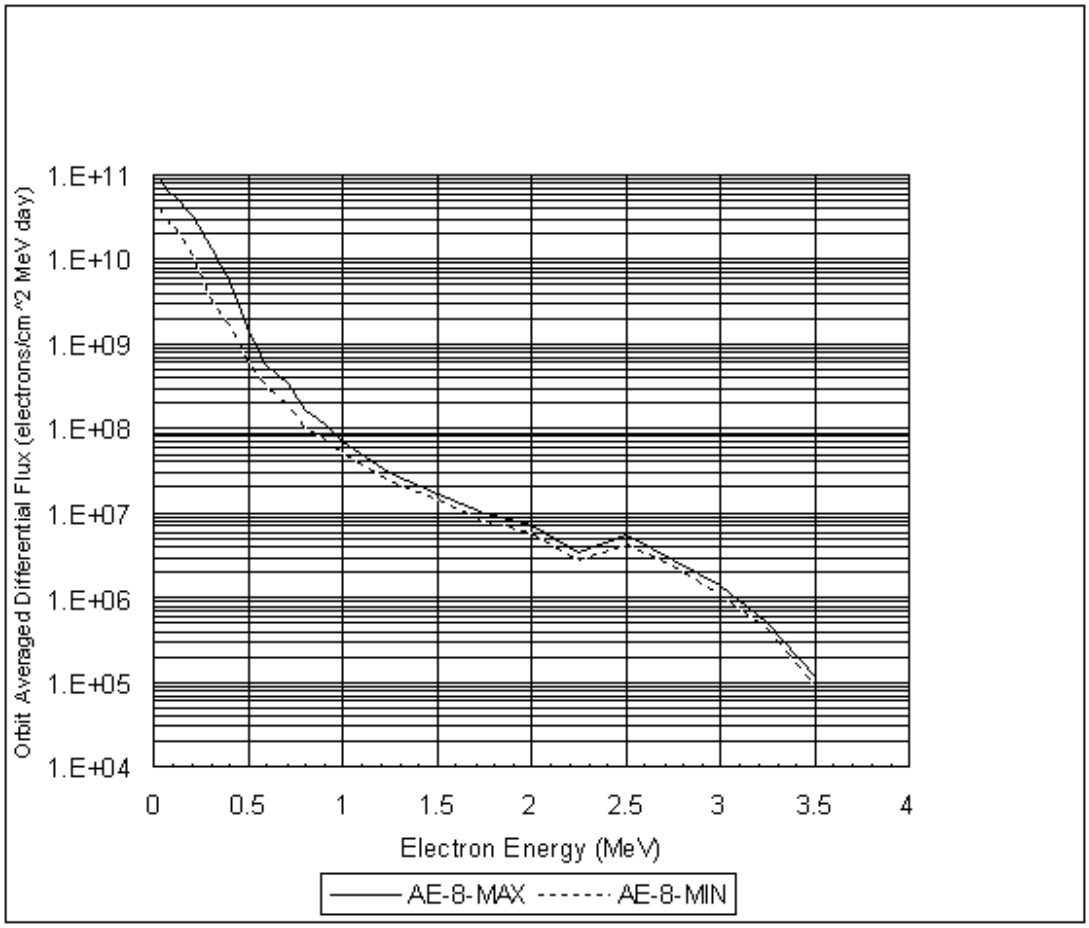

Figure 2: HST trapped electron spectra for solar maximum and solar minimum.

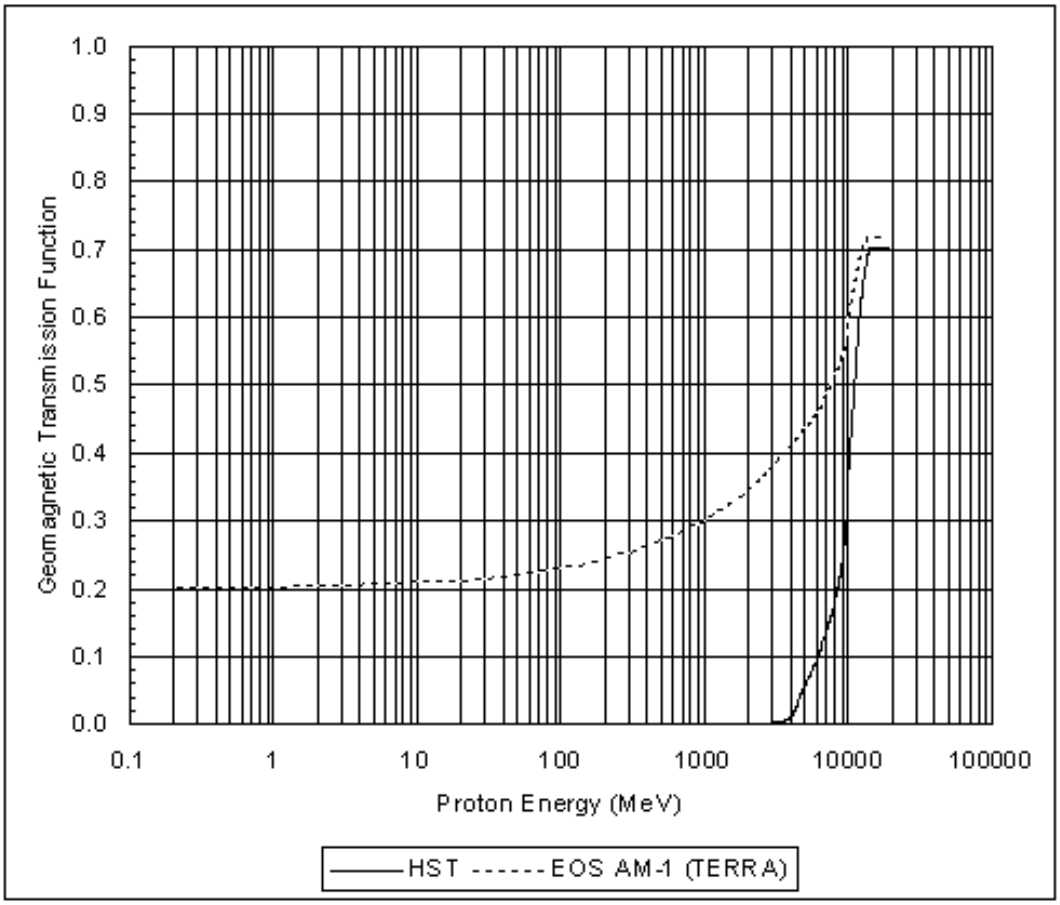

Figure 3: Geomagnetic transmission functions for HST and TERRA.

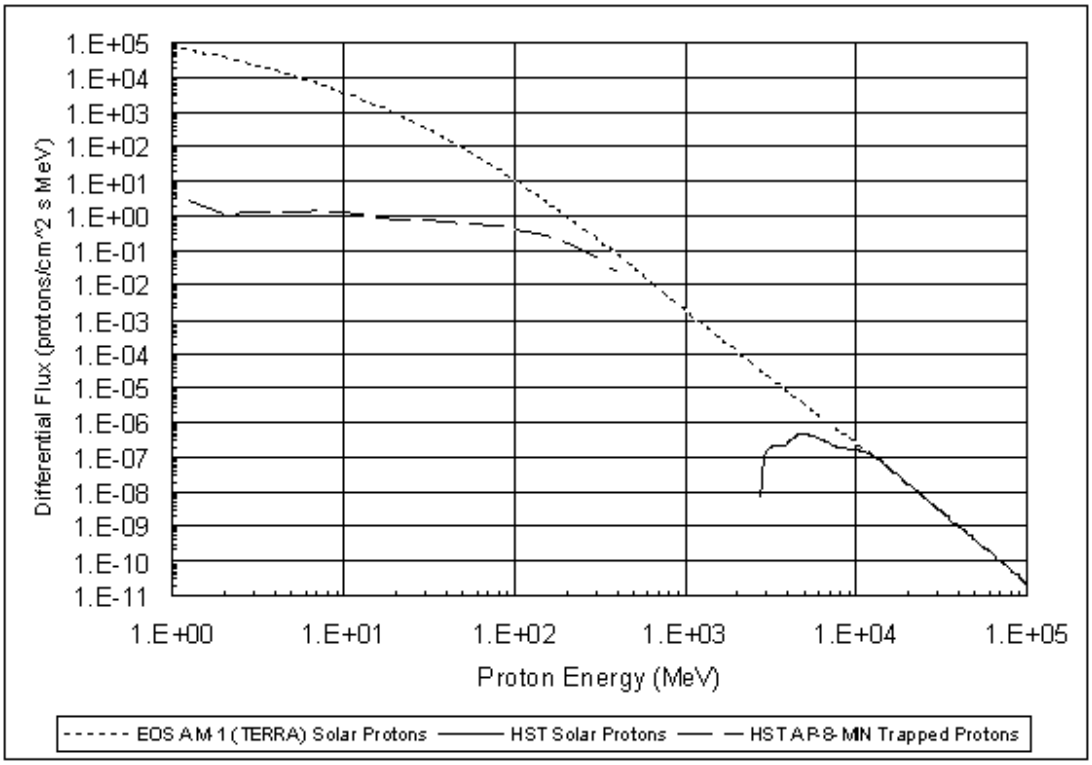

Figure 4: CME proton environment for HST and TERRA.

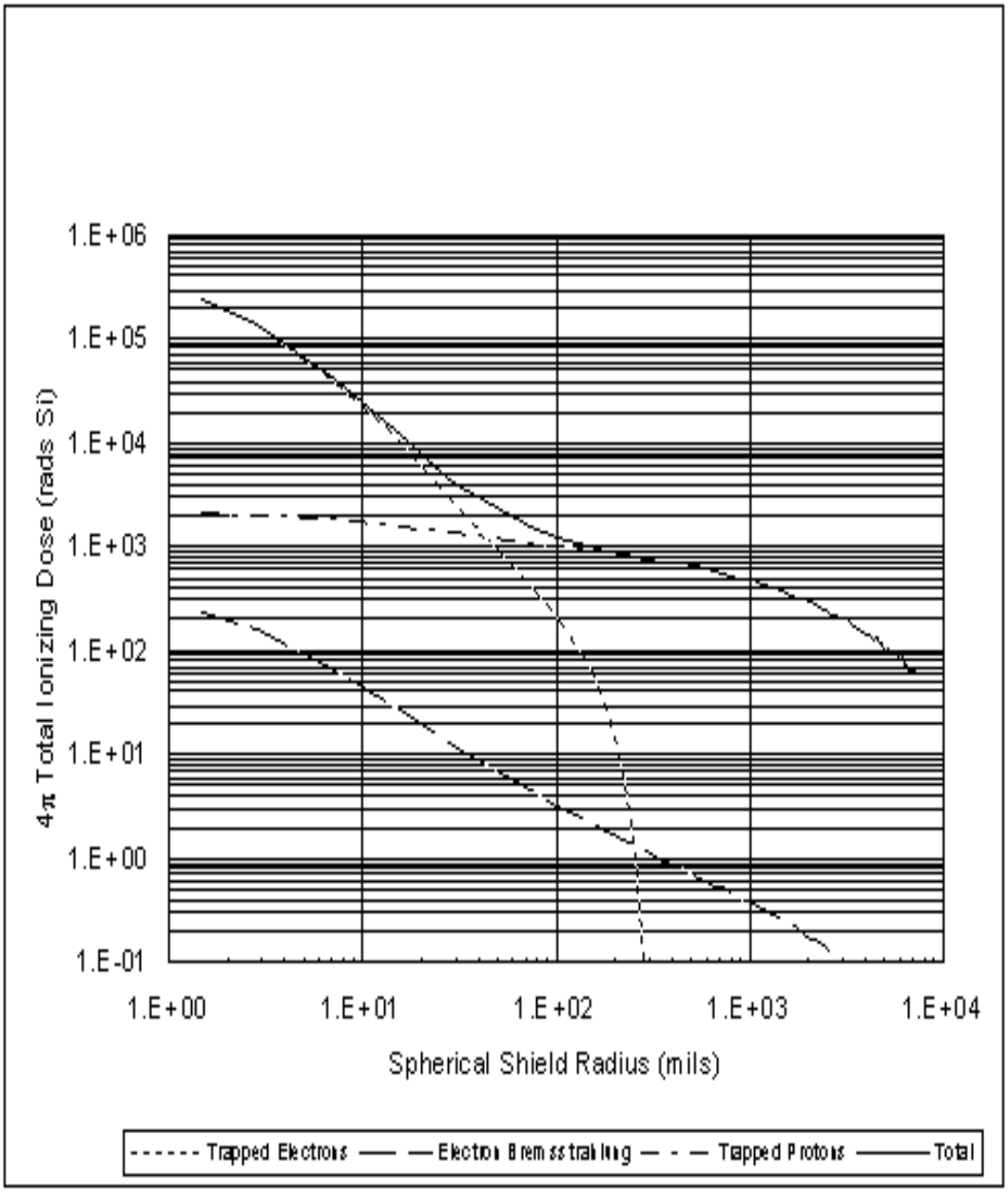

Figure 5: 2.5 year HST worst-case TID versus spherical aluminum shield thickness.

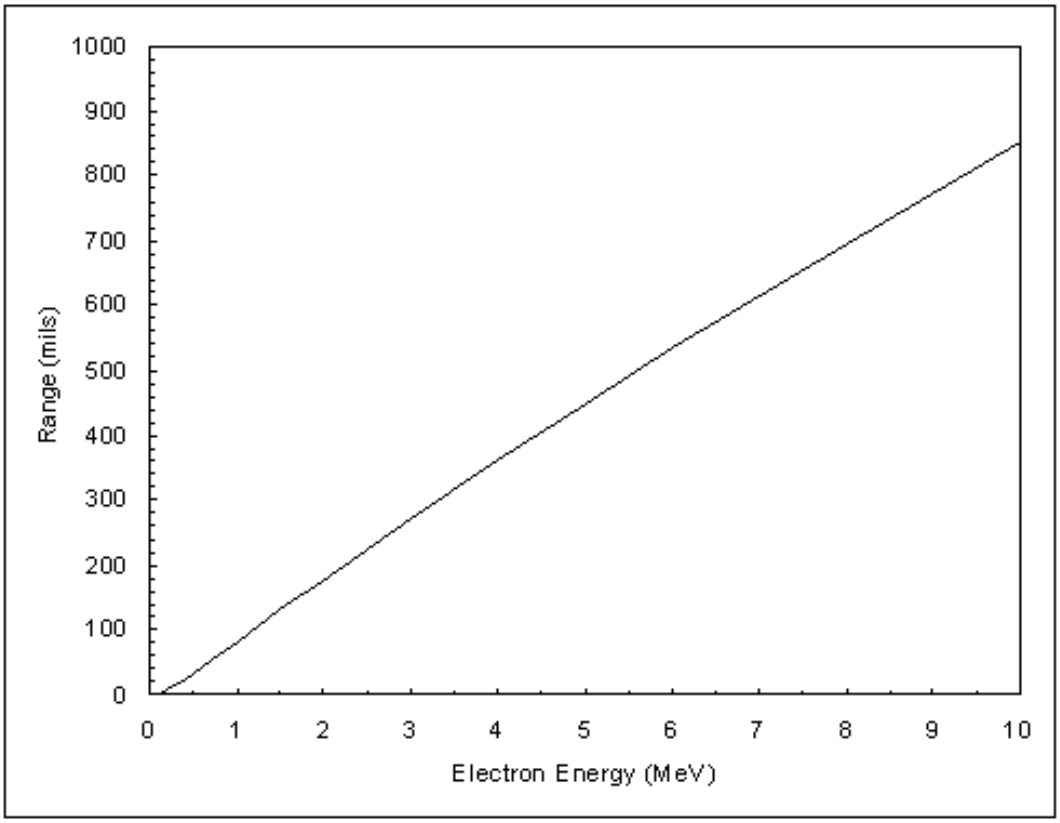

Figure 6: Electron range in aluminum.

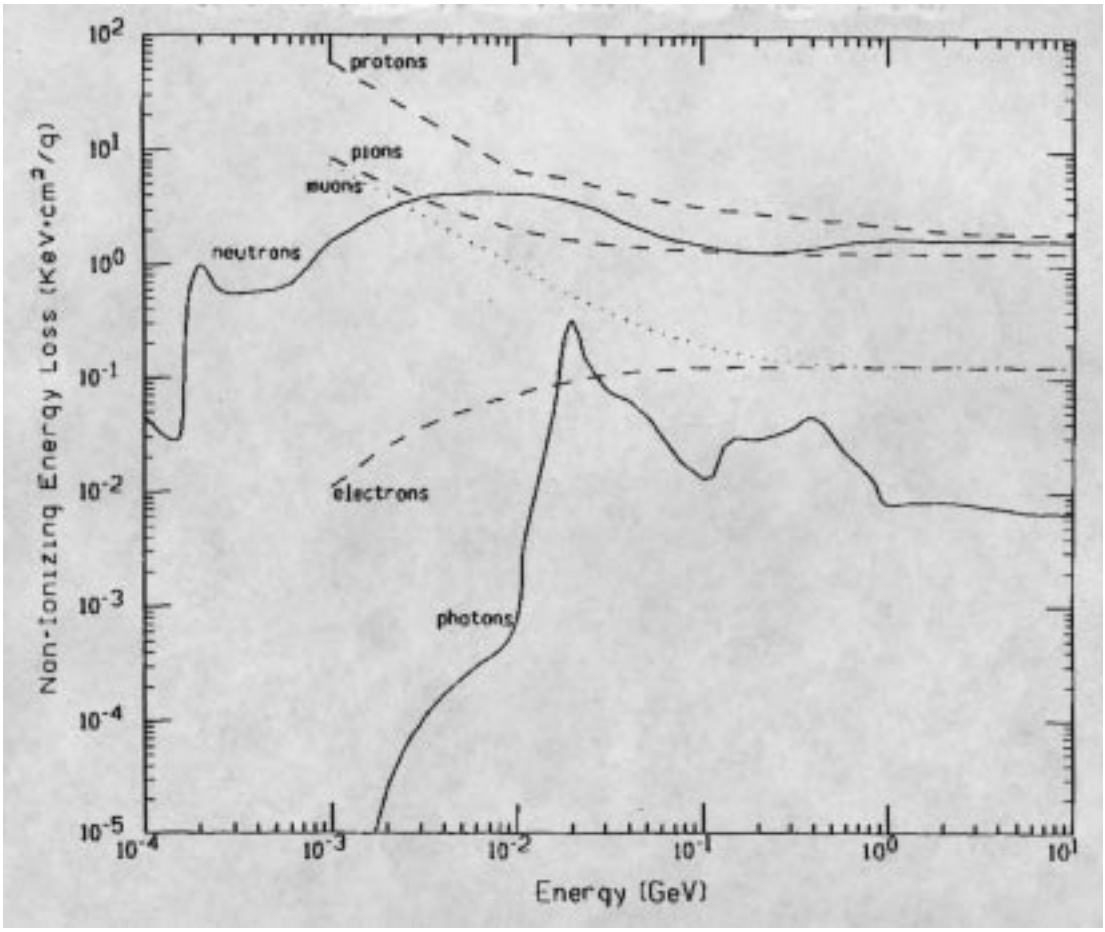

Figure 7: NIEL for silicon from Van Ginneken [19].

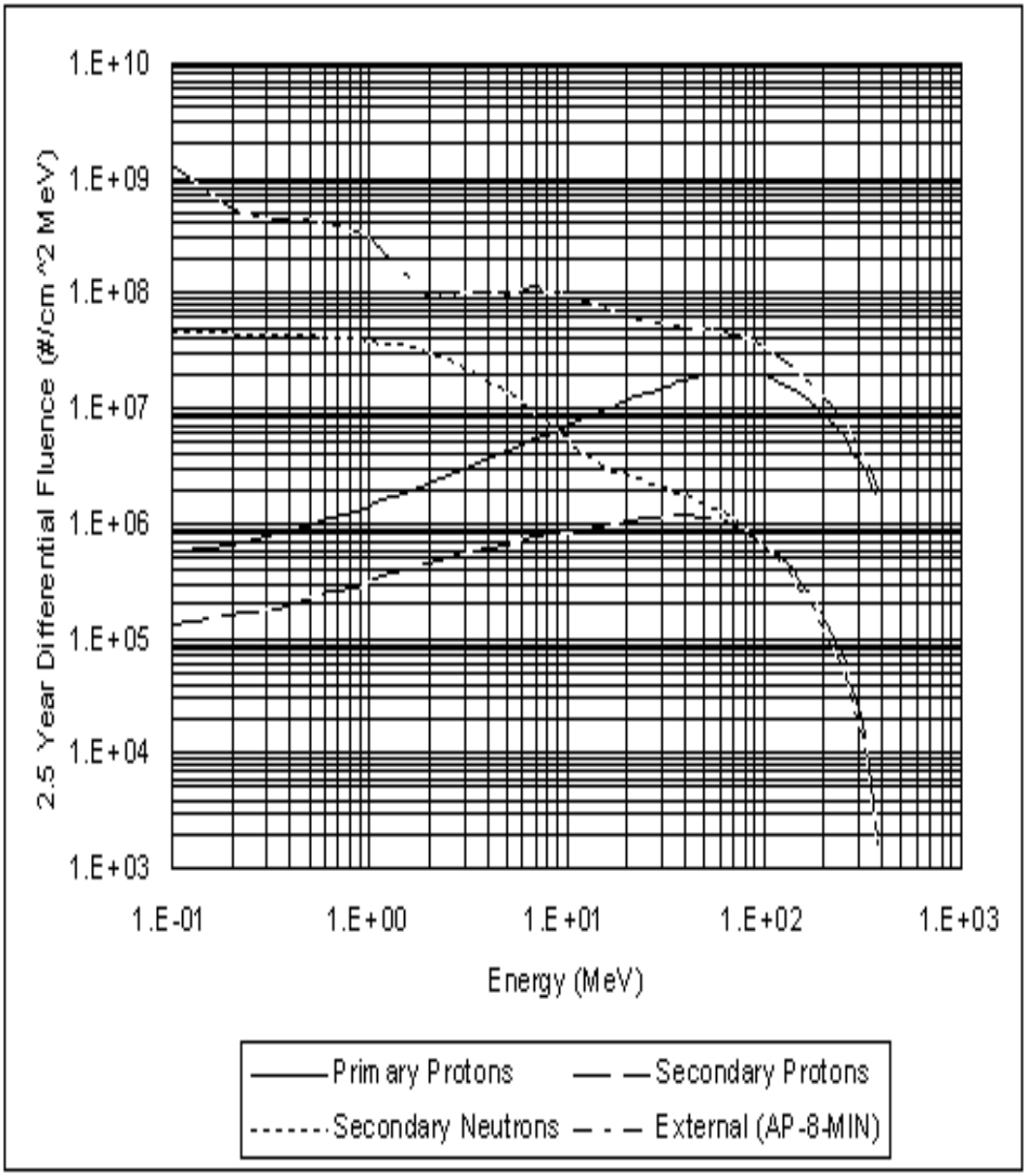

Figure 8: Exiting spectra after transport through 1 inch of spherical aluminum shielding.

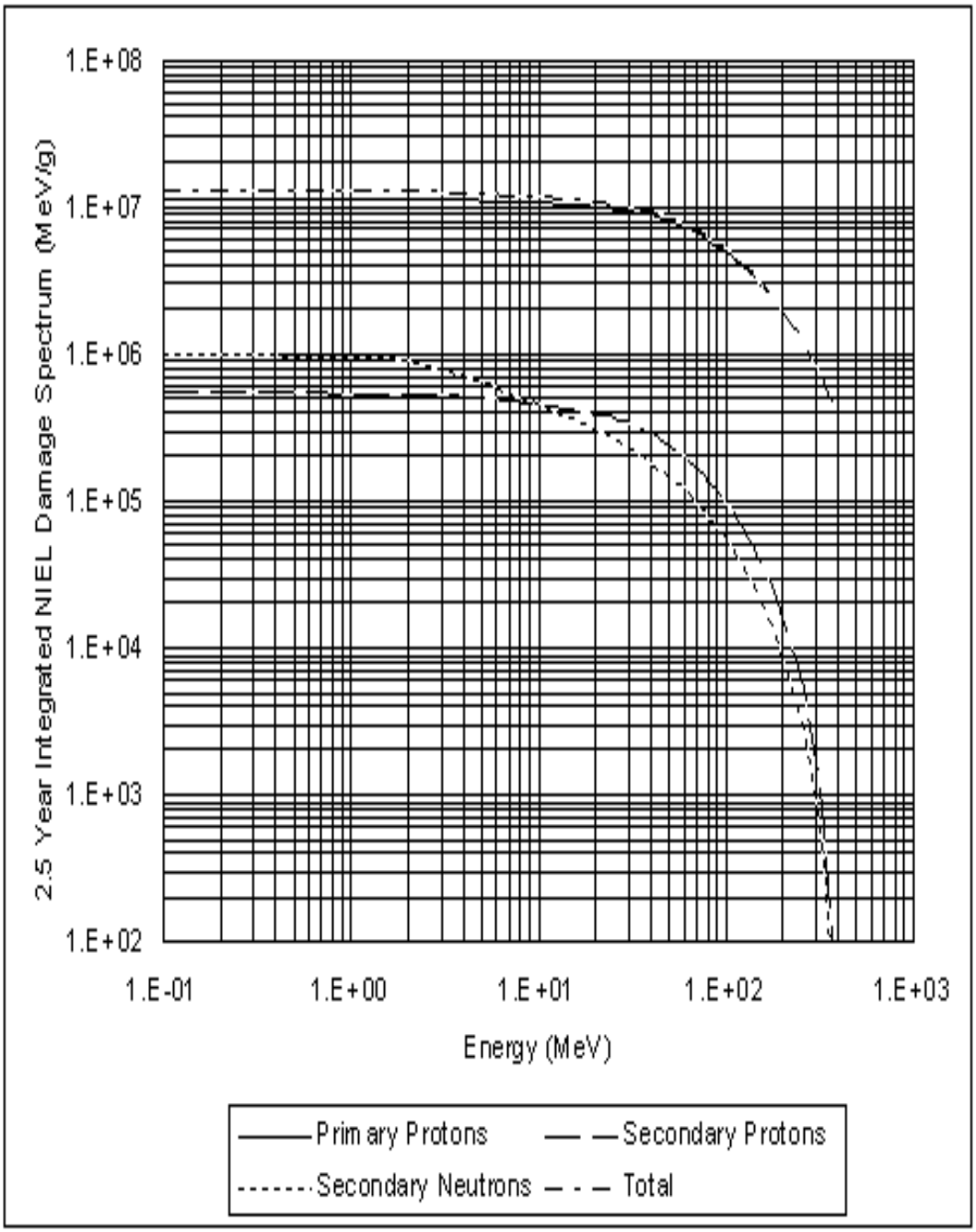

Figure 9: Integrated NIEL damge spectra for 1 inch of spherical aluminum shielding.

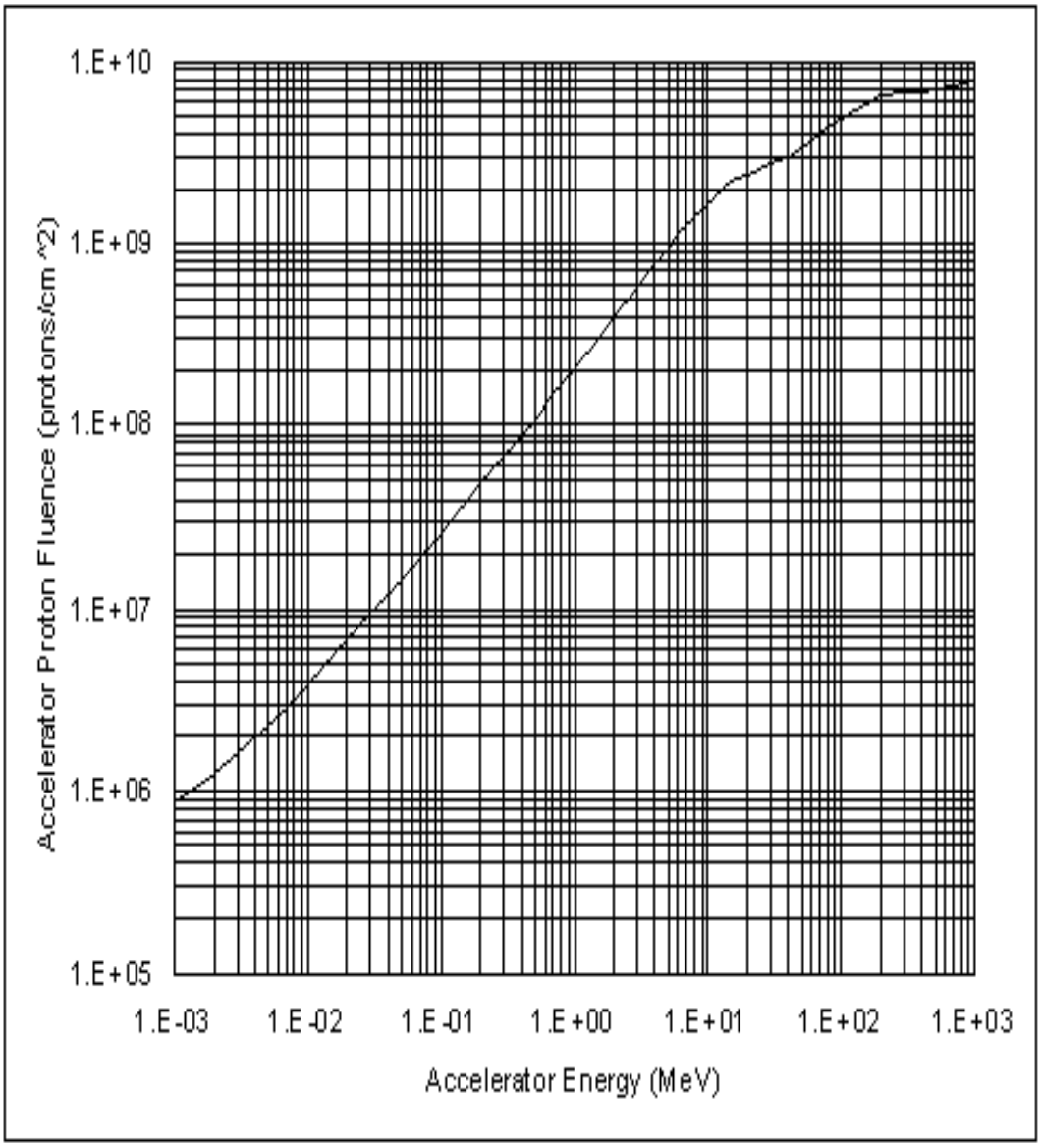

Figure 10: 2.5 year accelerator proton fluence.